JOURNAL OF PROPULSION AND POWER
Vol. 14, No. 2, March–April 1998

Measured Rotor Wake and Potential Forcing Functions, Including Blade Row Interactions

Robert T. Johnston,* John M. Feiereisen,† and Sanford Fleeter‡
Purdue University, West Lafayette, Indiana 47907

A fundamental experiment is directed at the acquisition and analysis of data defining compressible forcing functions generated by a rotor, including interactions with the upstream-generated inlet guide vane (IGV) wakes, for application to wake forcing function models in turbomachine forced-response design systems. The research fan facility consists of an IGV row and a downstream rotor. IGV–rotor axial spacing is variable, with the IGV row able to be indexed circumferentially, thereby enabling the rotor wakes to be measured both in the IGV freestream and wakes. At a rotor-relative Mach number of 0.6 unsteady measurements are made of the rotor wake pressure and velocity fields for two IGV–rotor axial spacings and with the rotor wake measured in the IGV freestream and wake regions. The decay characteristics of the rotor blade wakes are compared to empirical correlations. After Fourier decomposition, a vortical–potential gust splitting analysis is implemented and applied to the first-harmonic data to determine the vortical and potential harmonic wake gust forcing functions both upstream and downstream of the rotor. The potential gust component of the rotor wakes upstream of the rotor is found to be dominated by the first-harmonic component with small contributions from the second and third harmonics. Higher harmonics of the vortical gust component of the rotor wakes measured both in and out of the IGV wakes are found to be significantly reduced in the IGV wake regions.

Nomenclature

A_n = potential disturbance nth harmonic proportionality constant
C_R = rotor chord
D_n = vortical disturbance nth harmonic proportionality constant
$\boldsymbol{k}$ = gust wave number vector
M = Mach number
p = static pressure perturbation
S_R = rotor blade spacing
s = streamwise distance from rotor trailing edge
$\boldsymbol{U}$ = mean absolute velocity vector
u = axial velocity perturbation
u^+ = streamwise velocity peturbation
v = tangential velocity perturbation
v^+ = transverse velocity perturbation
$\bar{\boldsymbol{W}}$ = mean rotor-relative velocity vector
W_{dc} = wake streamwise centerline velocity defect
W_0 = freestream streamwise velocity
$\boldsymbol{w}$ = perturbation velocity vector
$\boldsymbol{x}$ = spatial coordinate, $\xi\hat{e}_\xi + \eta\hat{e}_\eta$
δ = semiwake width
η = transverse coordinate
ξ = axial coordinate
ξ_d = downstream distance measured from rotor trailing edge
ξ_u = upstream distance measured from rotor leading edge
$\bar{\rho}$ = mean density
ϕ_p = unsteady potential

Subscripts
c = combined vortical/potential
m = measured
n = nth harmonic
p = potential
r = relative coordinate system
v = vortical

Presented as Paper 94-2975 at the AIAA/ASME/SAE/ASEE 30th Joint Propulsion Conference, Indianapolis, IN, June 27–29, 1994; received April 5, 1996; revision received July 20, 1997; accepted for publication Aug. 21, 1997.

*Research Assistant, School of Mechanical Engineering. Member AIAA.
†Visiting Assistant Professor, School of Mechanical Engineering. Member AIAA.
‡McAllister Distinguished Professor, School of Mechanical Engineering. Associate Fellow AIAA.

Introduction

BLADE row–wake interactions are the most common and least understood source of unsteady aerodynamic excitation; they cause blade row vibrations that result in high-cycle blade fatigue. Linearized forced-response analyses first require a definition of the unsteady aerodynamic wake forcing function in terms of its harmonics before the unsteady aerodynamic response of the downstream blade row to each wake harmonic can be analyzed. A wake behind a blade results from the joining of the blade surface boundary layers at the trailing edge. This wake convects downsteam with the flow, and this velocity deficit region decays and spreads out with distance. Typically, experiments and the wake models developed from them have been directed at steady performance. Empirical wake models include those of Mugridge and Morfey,[1] and Lakshminarayana and Davino,[2] each of whom developed separate equations for the near- and far-wake regions. Majjigi and Gliebe[3] developed a linear rational model to describe wake behavior whereby only one equation was required for both the near- and far-wake regions. Additionally, numerical solutions of the Euler and Navier–Stokes equations are being applied to rotor–stator interactions. However, according to Chiang and Kielb,[4] such solutions are not practical at present for forced-response analyses because of their extensive computational requirements and the necessity for forced-response systems to analyze a relatively large number of conditions.

Turbomachines are designed with closely spaced blade rows to reduce weight. As a result, the use of wake forcing-function models for forced-response prediction is significantly limited. First, currently used wake forcing-function empirical or semi-

empirical models have been based on far-wake steady flow measurements from a single isolated airfoil row, often operated in the incompressible flow regime. Hence, these far-field wake data are not appropriate for closely spaced compressible Mach number blade rows. Second, the airfoil row generates a potential field because of its thickness and lifting properties in addition to a viscous wake. This potential field decays rapidly with distance but is significant for closely spaced blade rows. Finally, the experiments performed in cascades and the models derived from them do not account for streamline curvature effects present in a turbomachine.

Forced-response predictions are based on linearized two-dimensional inviscid cascade flow analyses where each wake harmonic gust forcing function is independently considered. These gust forcing functions consist of two components: 1) potential and 2) vortical disturbances. Potential disturbances extend both upstream and downstream, decay exponentially with distance, and would exist in the absence of viscosity. Vortical wakes convect downstream with the mean flow and result from viscous action at the blade surface. If the flow were inviscid, these vortical wakes would remain constant with time. Fundamental vortical gust forcing functions have been considered by Henderson and Fleeter,[5] and combined vortical–potential gust forcing functions were considered by Manwaring and Wisler[6] and Feiereisen et al.[7]

This paper addresses the limitations of wake forcing-function models used for forced-response prediction. In particular, an experiment is performed in the Purdue Research Axial Fan Stage directed at the acquisition and analysis of data defining forcing functions generated by a rotor, including interactions with the upstream-generated inlet guide vane (IGV) wakes, for application to turbomachine forced-response design systems. This facility, designed with an IGV row and a downstream rotor, is ideal for these wake forcing-function experiments because 1) it is large enough for the necessary high-quality measurements, 2) the IGV–rotor axial spacing is variable, and 3) the IGV row can be indexed circumferentially, thereby enabling the rotor wake data to be analyzed both in the IGV freestream and wakes, i.e., the IGV–rotor wake interactions can be investigated. At a rotor-relative Mach number of 0.6, unsteady measurements are made of rotor wake pressure and velocity fields using hot films and unsteady pressure probes. First, the decay characteristics of the rotor blade wakes for two IGV–rotor axial spacing values and with the rotor wakes in the IGV freestream and wake regions are compared to empirical correlations. Then, after Fourier decomposition, a vortical–potential gust splitting analysis is implemented. The vortical and potential harmonic wake gust forcing functions are determined both upstream and downstream of the rotor, and the effects of IGV axial spacing and IGV–rotor interactions are investigated.

Axial Fan Facility

The Purdue Research Axial Fan facility (Fig. 1) features a 30.48-cm (12-in.) diam, 2/3 hub-tip ratio design compressor rotor that is integral with the shaft. The drive system consists of a 300-hp ac motor driving a magnetic clutch with a variable speed output that drives a gearbox. Flow enters through a 16:1 contraction, then goes through a 4:1 contraction because of the centerbody. Eighteen inlet guide vanes are twisted to produce a free vortex whirl into a 19-blade axial flow rotor (Fig. 1). Both the inlet guide vanes and the rotor blades are designed with NACA 65 series airfoil sections on circular arc meanlines. The adjustable inlet guide vanes have a nominal 10% thickness with a chord varying from 35.5 mm (1.40 in.) at the hub to 53.3 mm (2.10 in.) at the tip to yield a solidity of one. Rotor blade sections have a 10–6% hub-to-tip thickness taper, with a chord of 50.8 mm (2.00 in.) and a blade-to-blade spacing of 42 mm (1.65 in.) at midspan. For these experiments, axial IGV-to-rotor spacing to chord ratios of $Z/C_R = 0.93$ and 1.18 are investigated. The IGV row is indexed circumferentially, thereby enabling measurements to be made in the IGV wake regions without complicated circumferential probe traverses upstream and downstream of the rotor. The turbulence intensity measured 26 mm upstream of the inlet guide vanes is 2.5%. The compressor is operated at 10,000 rpm for all tests, giving a total pressure ratio of 1.08 and typical mass flow rates of 3.8 kg/s (8.4 lb/s).

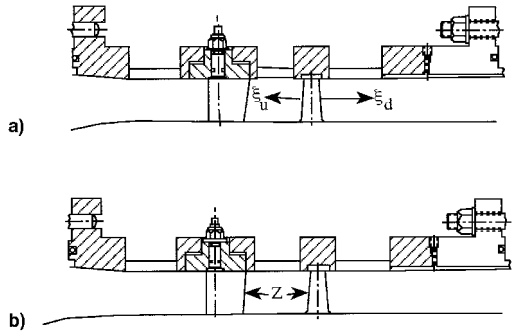

Fig. 1 Test compressor configuration: a) minimum IGV–rotor spacing $Z/C_R = 0.93$ and b) maximum IGV–rotor spacing $Z/C_R = 1.18$.

Unsteady velocity and static pressure fluctuations are measured at midspan both upstream and downstream of the rotor with hot film anemometers and unsteady pressure probes designed to access the confined regions downstream of the IGV row and rotor. An Endevco piezoresistive pressure transducer with a sensitivity of 59.85 mV/psi and a frequency response of 70 kHz has been used in the construction of a total pressure probe. This design is capable of ±17-deg misalignment to the flow with less than 1% error in total pressure. All probes are set to minimize flow angle deviations from the probe axis, with incident flow angle fluctuation errors of no more than 1%. The crossed hot film has a measurement area of 50.8 μm × 1.0 mm, with absolute velocity magnitude and flow angle errors estimated at 2% and 0.5 deg, respectively. The unsteady velocity and total pressure measurements are ensemble-averaged over 200 individual revolutions, triggered by a once-per-rev pulse from a photo-optic sensor, and are used to calculate the unsteady static pressure.

Unsteady Data Acquisition

The time-variant signals are digitized over 10 blade passages using approximately 2000 samples per burst. The Fourier components of the ensemble-averaged time traces are numerically determined using Fourier transform software. The sample frequency is used to produce time records of exactly one rotor revolution to eliminate frequency leakage problems. Sample frequency is set based upon the number of rotor blades, the desired number of data points per wake, and the rotor rotational speed measured with 16 bit counters on one A/D board.

Wake Correlation

The rotor blade wake decay characteristics are determined and compared with the empirical correlations developed by Majjigi and Gliebe[3] for the semiwake width δ and the wake centerline velocity defect W_{dc}. The correlation equations are

$$\frac{\delta}{S_R} = \frac{0.31875(s/C_R)C_D^{0.125} + 0.048}{0.268125(s/C_R)C_D^{0.125} + 1.0}$$

$$\frac{\delta}{C_R} = \frac{0.2375(s/C_R)C_D^{0.125} + 0.034125}{0.357(s/C_R)C_D^{0.125} + 1.0} \qquad (1)$$

$$\frac{W_{dc}}{W_0} = C_D^{0.25}\,\frac{0.3675(s/C_R) + 1.95}{7.65(s/C_R) + 1.0}$$

where C_D denotes the airfoil section drag coefficient.

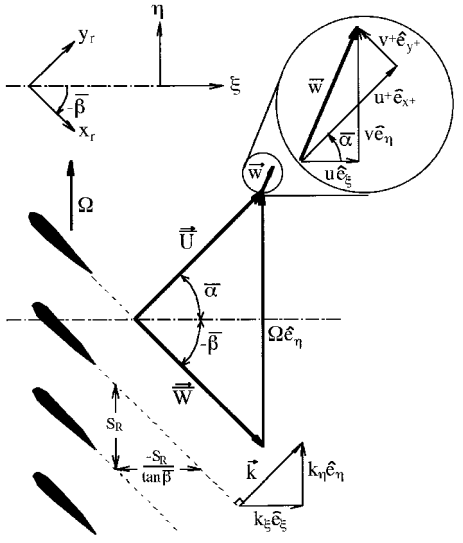

Fig. 2 Rotor wake flowfield.

Vortical–Potential Gust Splitting Analysis

The two-dimensional inviscid flow is assumed to be compressible, isentropic, and composed of an absolute mean velocity $\bar{\boldsymbol{U}}$ with superimposed small velocity $\boldsymbol{w}$ and perturbations p (Fig. 2). The linearized continuity and momentum equations are

$$\frac{1}{c_0^2}\frac{\bar{D}p}{Dt} + \bar{\boldsymbol{\rho}}\nabla\cdot\boldsymbol{w} = 0$$
$$\bar{\boldsymbol{\rho}}\frac{\bar{D}\boldsymbol{w}}{Dt} + \nabla p = 0 \tag{2}$$

Vortical–Potential Splitting

The perturbation velocity field is split into vortical and potential gust components $\boldsymbol{w} = \boldsymbol{w}_v + \boldsymbol{w}_p$, per Goldstein,[8] which satisfy

$$\frac{\bar{D}\boldsymbol{w}_v}{Dt} = 0, \qquad \nabla\cdot\boldsymbol{w}_v = 0 \tag{3}$$

$$\rho\frac{\bar{D}\boldsymbol{w}_p}{Dt} = -\nabla p, \qquad \frac{1}{\rho c_0^2}\frac{\bar{D}p}{Dt} = -\nabla\cdot\boldsymbol{w}_p, \qquad \nabla\times\boldsymbol{w}_p = 0 \tag{4}$$

Thus, the forcing function is analyzed harmonically as a Fourier series of individual vortical and potential gusts, $\boldsymbol{w}(\boldsymbol{x}, t) = \sum\{[\boldsymbol{w}_{vn}(\boldsymbol{x}) + \boldsymbol{w}_{pn}(\boldsymbol{x})]\}e^{i\omega t}$.

Vortical Gust

Spatial periodicity shows that the gust wave number vector must be perpendicular to $\boldsymbol{W}$

$$\boldsymbol{k}\cdot\boldsymbol{W} = 0 \tag{5}$$

where $\boldsymbol{W} = \bar{W}(\cos\bar{\boldsymbol{\beta}}\hat{e}_\xi + \sin\bar{\boldsymbol{\beta}}\hat{e}_\eta)$.

Periodicity requirements determine the tangential wave number $k_\eta = 2\pi/S_R$, with the axial wave number then determined from Eq. (5), $k_\xi = -k_\eta\tan\bar{\beta}$. The vortical gust convects with the mean flow $\boldsymbol{W}$. This condition and $\nabla\cdot\boldsymbol{w}_v = 0$ relate the wave number vector and the gust amplitude vector such that the gust is oriented in a direction normal to $\boldsymbol{w}_{vn}$. Combining this with Eq. (5) shows that the vortical gust amplitude vector must be parallel to the mean velocity. Denoting the complex constant of proportionality between these two constant vectors by D_n^* leads to

$$\boldsymbol{w}_{vn} = D_n^*\bar{W}(\cos\bar{\beta}\hat{e}_\xi + \sin\bar{\beta}\hat{e}_\eta)\exp\{-in\boldsymbol{k}\cdot\boldsymbol{x}\} \tag{6}$$

Thus, the vortical gust propagates unattenuated in the direction of $\boldsymbol{k}$. This defines the vortical gust velocity perturbation with all parameters known from measurements with the exception of D_n^*, which must be calculated for each harmonic.

Potential Gust

The potential gust $\boldsymbol{w}_p$ can be derived from a potential function, $\boldsymbol{w}_p = \nabla\phi_p$ and, therefore, must satisfy $\nabla\times\boldsymbol{w}_p = 0$. The perturbation potential is related to p through the unsteady Bernoulli equation. Substituting these relations into Eq. (5) yields the following perturbation velocity potential equation:

$$\frac{1}{c_0^2}\frac{\bar{D}}{Dt}\left(\frac{\bar{D}\phi_p}{Dt}\right) - \nabla^2\phi_p = 0 \tag{7}$$

Because the flow is steady, the potential gust solution, determined from the steady form of this equation, is

$$\phi_{pn} = A_n\exp[n(\chi k_\eta\xi - ik_\eta\eta)] \tag{8}$$

where

$$\chi = \frac{-iM_r^2\sin\bar{\beta}\cos\bar{\beta} \pm \sqrt{1 - M_r^2}}{1 - M_r^2\cos^2\bar{\beta}}$$

is the axial decay factor and A_n is a complex constant.

Thus, the potential gust is periodic in the tangential direction but decays exponentially in the axial direction. The direction of this axial decay depends on whether an upstream or downstream blade row is being analyzed. The potential static pressure perturbation is found from the unsteady Bernoulli equation

$$\frac{p_{pn}}{\rho\bar{U}^2} = A_n^*(-\chi\cos\bar{\beta} + i\sin\bar{\beta})\exp[n(\chi k_\eta\xi - ik_\eta\eta)] \tag{9}$$

Experimental Determination of D_n^* and A_n^*

The potential gust $\boldsymbol{w}_{pn}$ is irrotational. Therefore, the vorticity $\boldsymbol{\gamma}_{pn}$ is zero, $|\boldsymbol{\gamma}_{pn}| = |\nabla\times\boldsymbol{w}_{pn}| = 0$, and p_{pn} is given in Eq. (9). Thus, the potential gust manifests itself in both static pressure and velocity perturbations but not in the vorticity perturbation. The vorticity of the vortical gust is

$$|\boldsymbol{\gamma}_{vn}| = |\nabla\times\boldsymbol{w}_{vn}| = D_n^*\frac{\text{in}\,k_\eta\bar{U}}{\cos\bar{\beta}}\exp\{-in\boldsymbol{k}\cdot\boldsymbol{x}\}$$

and there is no corresponding static pressure perturbation. Therefore, this vortical gust component manifests itself in a vorticity perturbation but no static pressure perturbation.

The static pressure perturbation is dependent only on the potential gust. At the measurement location $(\xi, \eta) = (0, 0)$, the potential gust coefficient A_n^*, computed explicitly from the static pressure, is

$$A_n^* = \frac{p_{mn}}{\rho\bar{U}^2(-\chi\cos\bar{\beta} + i\sin\bar{\beta})} \tag{10}$$

where p_{mn} is the measured nth harmonic static pressure perturbation.

The potential gust velocity perturbation is then calculated and subtracted from the measured velocity perturbation to yield a difference velocity perturbation. Because the vorticity of the potential component is zero, the perturbation of the velocity difference has the same vorticity as the measured gust. Thus, the linear theory vortical gust coefficient is calculated from this difference velocity perturbation as

$$D_n^* = (1/\bar{U})(u_{dn}\cos\bar{\beta} + v_{dn}\sin\bar{\beta}) \tag{11}$$

Axial and tangential unsteady velocity components are then used to compute the streamwise and transverse components of the vortical and potential unsteady velocity fields with the following coordinate transform:

$$\begin{Bmatrix} u^+ \\ v^+ \end{Bmatrix} = \begin{bmatrix} \cos \bar{\alpha} & \sin \bar{\alpha} \\ -\sin \bar{\alpha} & \cos \bar{\alpha} \end{bmatrix} \begin{Bmatrix} u \\ v \end{Bmatrix} \tag{12}$$

Results

An experiment performed in the Purdue Research Axial Fan Stage was directed at the acquisition and analysis of data defining forcing functions generated by the rotor, both vortical and potential, including interactions with the upstream-generated IGV wakes, for application to turbomachine forced-response design systems. Data defining the rotor wake are acquired and analyzed for two IGV–rotor axial spacings (Z/C_R = 0.93 and 1.18) and in the IGV freestream and wake regions. The latter are accomplished by positioning the fixed hot film and unsteady pressure probes in the IGV freestream and wake regions where the IGV wakes are apparent as a region with reduced mean flow velocity. The rotor inlet absolute Mach number is 0.3 and the rotor relative Mach number is 0.6 at midspan.

Rotor Wake Correlations

The rotor wake data for the two IGV–rotor axial spacings are compared with the empirical Majjigi and Gliebe correlations[3] for δ and W_{dc} in Figs. 3 and 4, respectively. Noticeable differences between the measured δ and the correlation in the near rotor wake region exist. The measured semiwake width is generally larger and the velocity deficit is smaller than that predicted by the correlations. In the far-wake region, the δ/C_R and W_{dc}/W_0 data exhibit excellent agreement with the empirical correlation, whereas relatively poor agreement exists between

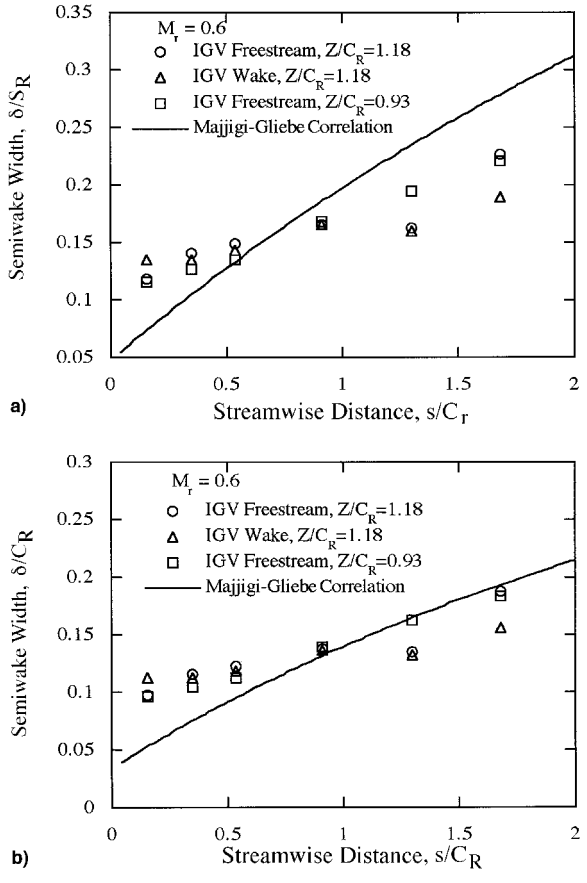

Fig. 3 IGV–rotor spacing and IGV wake effect on semiwake width correlation: a) δ/S_R and b) δ/C_R

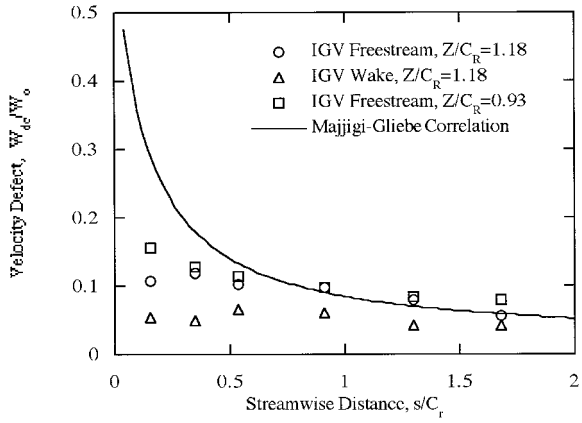

Fig. 4 IGV–rotor spacing and IGV wake effect on velocity deficit correlation: a) δ/S_R and b) δ/C_R

the δ/S_R data and the empirical correlation. IGV–rotor axial spacing changes have no effect on the rotor wake velocity deficit, but the increased axial spacing results in a small semiwake width increase. The standard deviation of the δ/C_R data from the correlation is 0.023, and the maximum value of the y coordinate is 0.188, which yields a normalized standard deviation of 12%. The standard deviation of the W_{dc}/W_0 data from the correlation is 0.064, yielding a normalized standard deviation of 41%. This large discrepancy between the correlation and the experimental values for the W_{dc}/W_0 is attributed to the poor agreement in the region near the rotor trailing edge. The effects of the upstream IGV wake interactions with the downstream rotor wakes for the larger IGV–rotor axial spacing are compared with the results from the empirical correlations of Majjigi and Gliebe in Figs. 3 and 4. Again, the data are noticeably different from the correlation in the near rotor wake region, with the measured δ generally larger and the velocity deficit smaller than those predicted by the correlation. Figure 3 illustrates that the far-field semiwake width is underpredicted by the correlation for δ/S_R, but the correlation for δ/C_R shows better agreement. The measured wake velocity deficit is in good agreement with the empirical correlation in the far field. The IGV–rotor wake interaction has a large effect on the rotor wake velocity deficit. Namely, the rotor wake velocity deficit is greatly reduced by the IGV wake in both the rotor near- and far-wake regions, although somewhat greater in the near-wake region. The reduction in the wake velocity deficit measured in the IGV wakes is attributed to the rotor blades having either earlier transition or separation in the IGV wake region. Higher rotor-to-rotor variations in the flow in the IGV wake region would lead to a smoothing of the ensemble-averaged signal, but the observation of the signals on an oscilloscope indicated that a reduction in the velocity deficit existed in the IGV wake region. This finding agrees with measurements taken by Walker and Oliver.[9] However, the nondimensional wake width is essentially unchanged by the IGV wakes. This result is attributed to the rotor blade wakes being rather long and narrow; therefore, changes in the magnitude of the velocity defect have little effect on the semiwake width.

Figure 5 illustrates the measurements of δ/C_R for the three cases studied along with a straight-line curve fit. The semiwake width for the results in the freestream at two different axial spacings are in good agreement and increase linearly. The semiwake width of the rotor wakes in the IGV wake region increases linearly, but at a lower rate (slope) than that measured in the IGV freestream.

Vortical–Potential Gusts

With positive pressure plotted to the left, Fig. 6 shows the unsteady velocity and static pressure for the maximum IGV–rotor axial spacing at nine axial locations upstream and six axial locations downstream of the rotor. The axial and tangen-

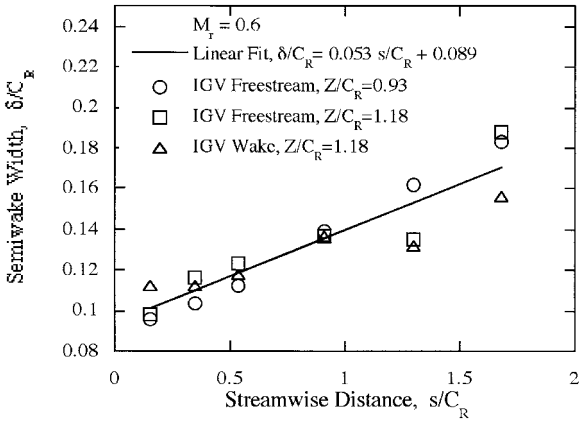

Fig. 5 IGV semiwake width shown with a linear curve fit.

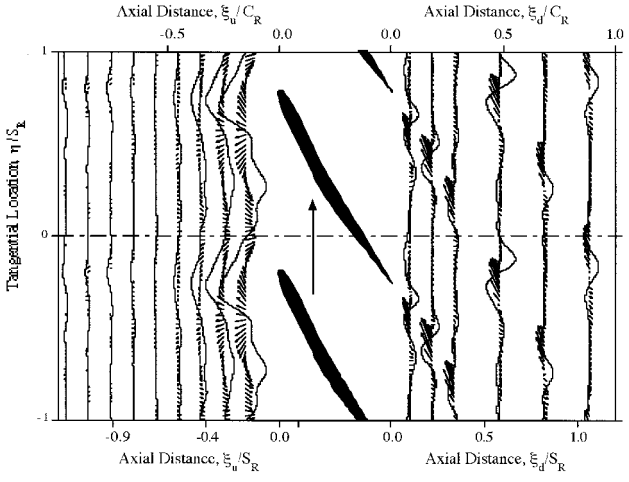

Fig. 6 Rotor-generated unsteady flowfield upstream and downstream of the rotor.

tial coordinates are nondimensionalized by the characteristic length for the wake analysis, the rotor blade-to-blade spacing S_R. For reference, the axial coordinate is also nondimensionalized by C_R. The axial coordinate origin for the data upstream of the rotor is the rotor leading edge, and the axial coordinate origin for the data downstream of the rotor is the rotor trailing edge. The unsteady velocity and pressure perturbations are very small far upstream of the rotor and grow exponentially as the rotor is approached. Downstream of the rotor, the narrow viscous wakes are clearly visible. The unsteady static pressure perturbations shown are calculated from the unsteady velocity and total pressure measurements assuming isentropic flow. As a result, any misalignment of the velocity and total pressure data or any total pressure losses (nonisentropic effects) result in an apparent unsteady static pressure.

Figure 7 shows the upstream data nearest the rotor. Note that the gust wave number vector is a concept as valid upstream of the rotor as downstream of the rotor. Thus, the gust plot is constructed along the wave number vector in a manner identical to that downstream of a rotor. The unsteady static pressure perturbation is quite large in comparison to the unsteady velocity perturbation. The magnitude and phase of the first-harmonic streamwise-to-transverse gust component ratio u_m^+/v_m^+ are 0.9790 and 94.3 deg, respectively. Hence, the unsteady velocity vector traces out an almost perfect circle that rotates counterclockwise with time. A circular point plot is characteristic of a predominantly potential flow.

Figure 8 depicts the downstream data nearest the rotor. The unsteady static pressure perturbation is small in comparison to the unsteady velocity perturbation. The magnitude and phase of the first-harmonic streamwise-to-transverse gust component ratio u_m^+/v_m^+ are 0.1264 and -112.6 deg, respectively. Thus, the unsteady velocity vector traces out a highly eccentric ellipse and rotates clockwise with time. A narrow elliptical point plot is characteristic of a predominantly vortical flow.

The results of applying the splitting analysis to the upstream and downstream data nearest the rotor are shown in Figs. 9 and 10. The gust is predominantly vortical downstream of the

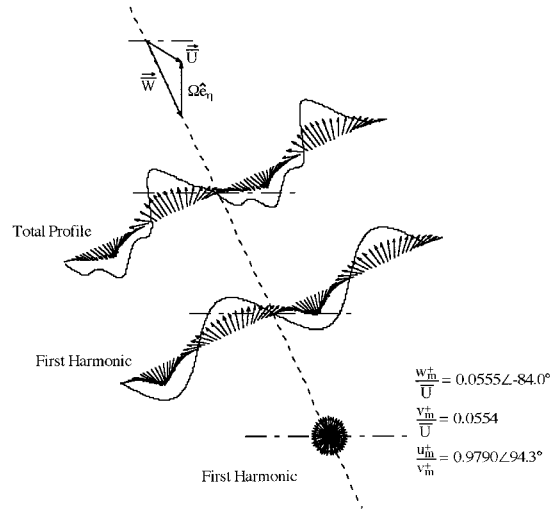

Fig. 7 Measured gust immediately upstream of the rotor.

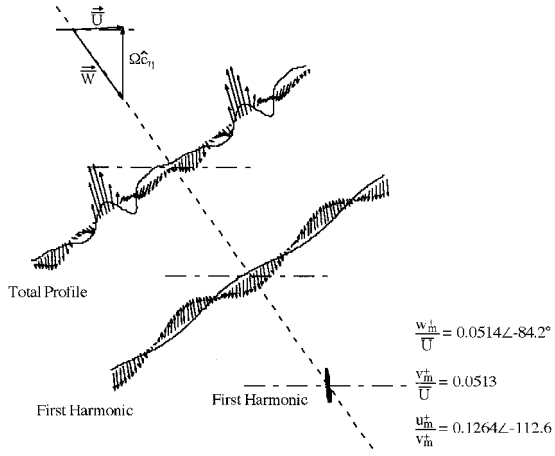

Fig. 8 Measured gust immediately downstream of the rotor.

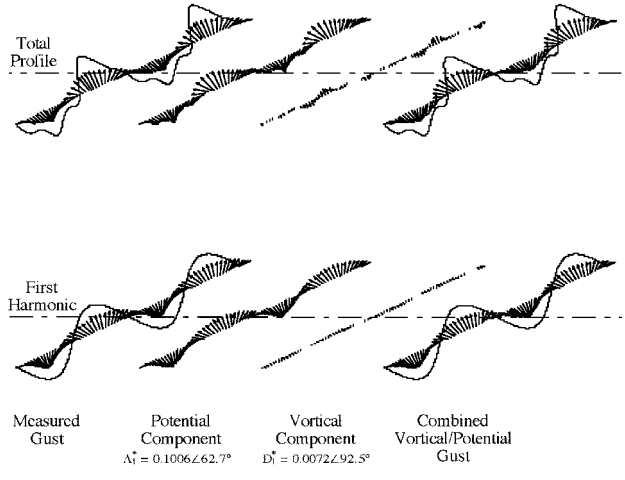

Fig. 9 Splitting analysis applied to the gust immediately upstream of the rotor.

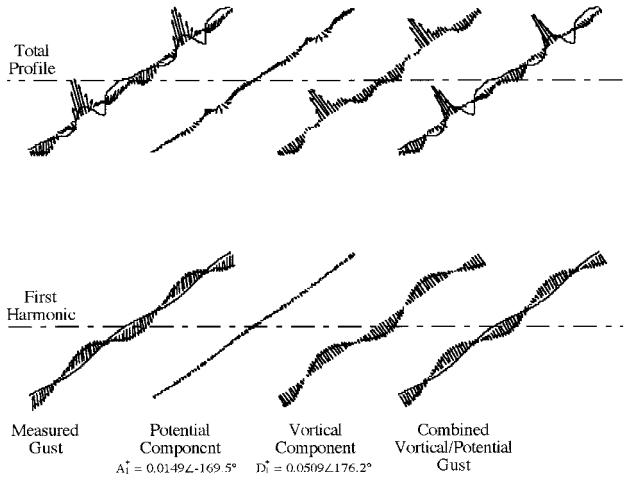

Fig. 10 Splitting analysis applied to the gust immediately downstream of the rotor.

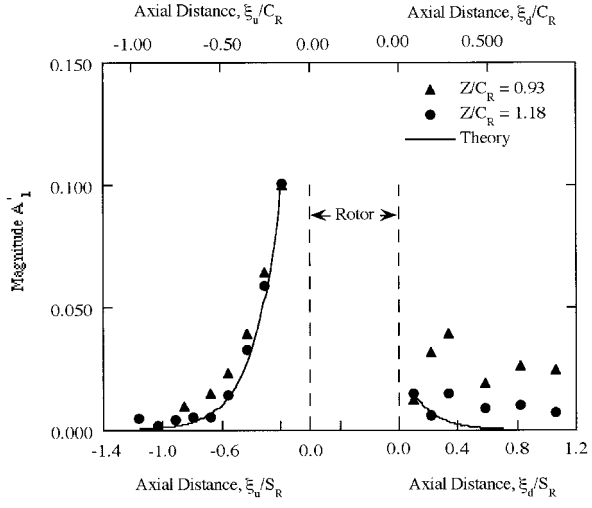

Fig. 11 IGV–rotor axial spacing effect on the potential gust axial variation.

rotor; whereas the upstream unsteady velocity perturbation is predominantly potential. Of course, no vorticity generated by the rotor can convect upstream to the measurement location, but the splitting indicates a small vortical component. This result is believed to be the result of a combination of factors: measurement error, misalignment of the probes used to measure velocity and total pressure, total pressure losses, and any propagating acoustic pressure waves.

Axial Gust Behavior

The axial behavior of the first-harmonic potential gust component calculated by the splitting analysis and specified by the value of A_1^* is shown in Fig. 11. The theory line is calculated by decaying the first value of A_1^* at the rate predicted by the theory and agrees well with the measured results. Potential effects are quite strong immediately upstream of the rotor and relatively small immediately downstream. This phenomenon is from the stagnation point at the blade leading edge, whereas the flow leaves the trailing edge relatively smooth. The nonzero value of A_1^* in the far field is attributed to a combination of probe misalignments, nonisentropic flow effects, and propagating acoustic waves.

Figure 12 shows the axial behavior of the rotor wake first-harmonic vortical gust component calculated by the splitting analysis and specified by the value of the magnitude of the vortical gust constant D_1^*. As predicted by the theory, D_1^* is relatively constant in the far-wake region, although there is a linear decrease in the value of D_1^* near the rotor.

The effects of the IGV–rotor axial spacing on the axial behavior of the rotor nondimensional first-harmonic vortical and potential gust components, specified by the values of the vortical and potential gust constants D_1^* and A_1^*, are shown in Figs. 11 and 12. Potential effects are quite strong immediately upstream of the rotor and relatively small immediately downstream. Decreasing the IGV–rotor spacing increases the magnitude of A_1^*, both upstream and downstream of the rotor, but has a much larger effect downstream. Upstream of the rotor, the theoretical rate of decay of the magnitude of A_1^* is shown for the maximum spacing and is in excellent agreement with the theory. However, downstream of the rotor, the values of A_1^* exhibit relatively poor correlations with the theory for both IGV–rotor axial spacings. Note that the theory predicts that the far-field potential gust will decay to zero; whereas, the data do not. This nonzero far-field potential was observed in the far-field data of Fig. 6 as the small unsteady static pressure field and is attributed to the fact that the static pressure perturbation was calculated using the unsteady total pressure and velocity assuming isentropic flow. Propagating acoustic modes caused by the IGV–rotor interaction may also be a contributing factor to this nonzero potential.

The magnitude of the vortical gust constant D_1^* is again relatively constant in the far-field wake region, as predicted by

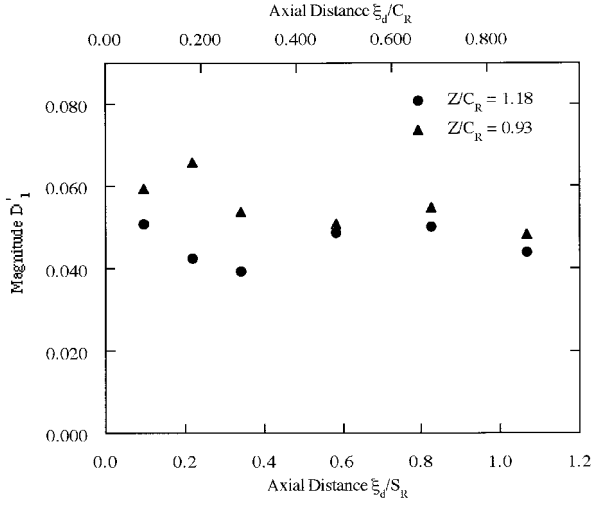

Fig. 12 IGV–rotor axial spacing effect on the vortical gust axial variation.

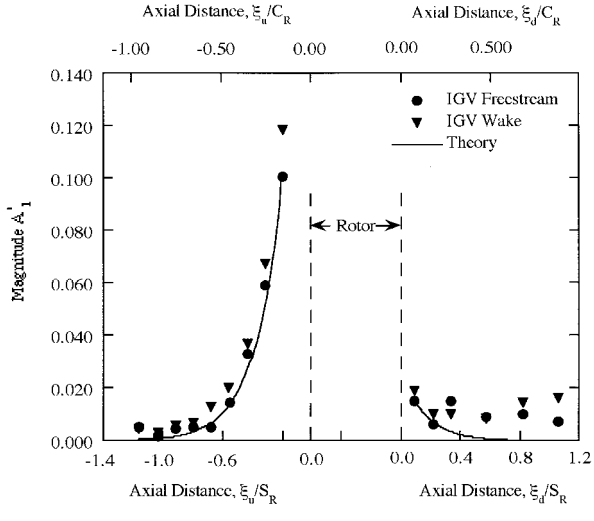

Fig. 13 IGV wake effect on the rotor potential gust axial variation.

the theory. However, it is not constant for either spacing near the rotor. Also, decreasing the IGV–rotor axial spacing results in an increase in the magnitude of the vortical gust D_1^*, particularly in the near-wake region.

The effects of the IGV wake on the axial behavior of the nondimensional first-harmonic vortical and potential gust components of the downstream rotor wakes are shown in Figs. 13 and 14. With regard to the rotor potential gust component, the IGV wakes have only a small effect on the axial behavior of A_1^*, both upstream and downstream of the rotor. The IGV wakes have a significant effect on the rotor vortical gust component, with the first-harmonic magnitude of D_1^* much larger in the IGV freestream than in the IGV wake region in both

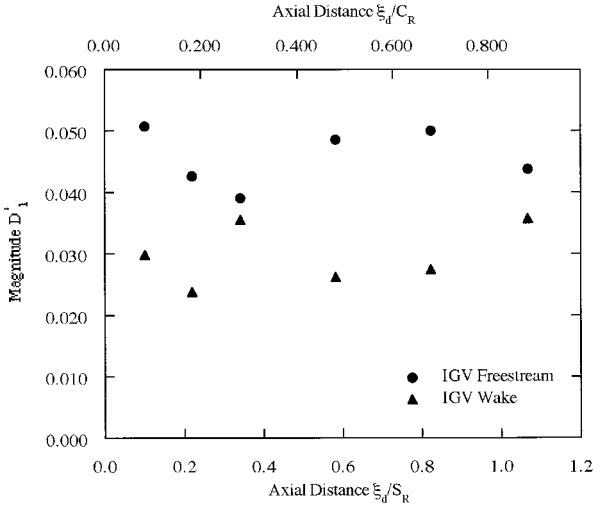

Fig. 14 IGV wake effect on the vortical gust axial variation.

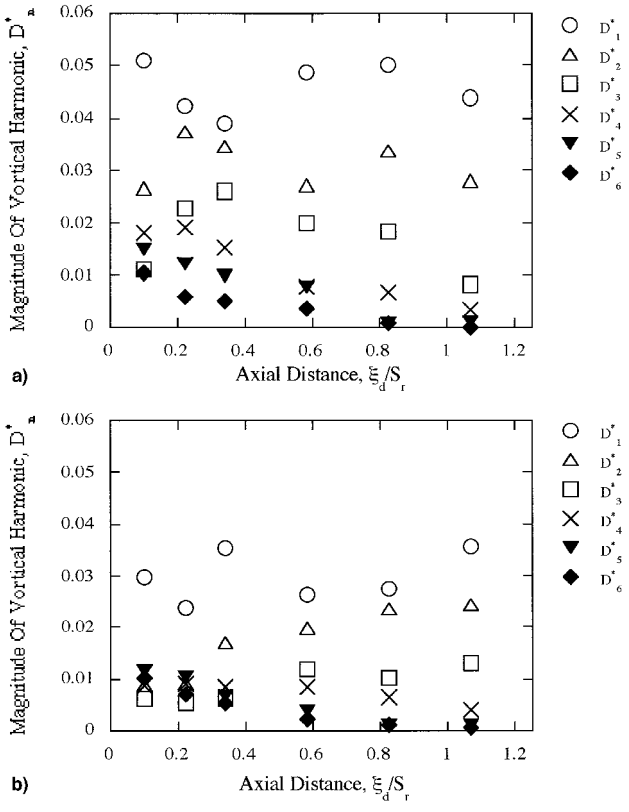

Fig. 15 Effect of the IGV wake on the harmonics of the rotor wake vortical component. Rotor wake vortical component measured in the IGV a) freestream and b) wake regions.

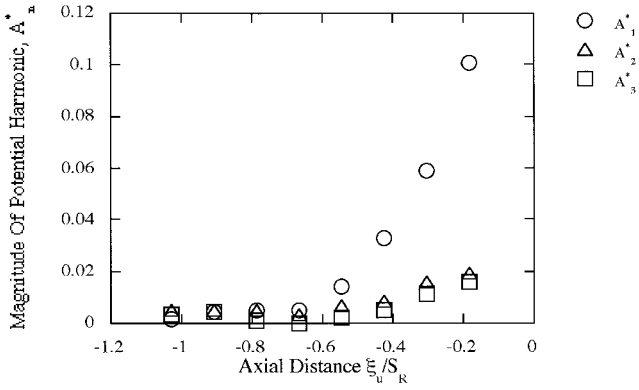

Fig. 16 Higher harmonics of the rotor wake potential component measured in the IGV freestream region.

the near- and far-wake regions of the rotor. In both the IGV wake and freestream, the magnitude of the vortical gust is relatively constant, as predicted by the theory, but fluctuates more nearer to the rotor in both the IGV wake and freestream.

The effect of the IGV wakes on the rotor wakes can also be seen in the axial behavior of the higher harmonics of nondimensional vortical gust components (Fig. 15). The IGV wakes have a significant effect on all of the rotor vortical gust harmonics, with the rotor vortical gust magnitude D_n^* much larger in the IGV freestream than in the IGV wake region for all harmonics plotted. Both in the IGV wake and freestream, the vortical gust magnitude of the first two harmonics is relatively constant, as predicted by the theory. This reduction in the harmonics of the vortical gust magnitude in the IGV wake region is attributed to earlier transition or blade separation which would result in a loss in lift, thereby reducing the shed vorticity in the wake. The higher harmonics (above the third) decay as a result of viscous diffusion that would not be present if the flow was inviscid. A slight increase in the magnitude of the first two harmonics of the vortical gust in the region of ξ_d/S_R = 0.6 to 0.8 can be explained as the transfer of energy from the higher harmonics to the lower harmonics as the wakes decay. After ξ_d/S_R = 0.8, the harmonics above three have become zero, and the lower harmonics begin to decay in the measurements from the IGV freestream region. In the IGV wake region, the fourth to sixth harmonics have not become zero until ξ_d/S_R = 1.1, and so the first three harmonics continue to increase. This energy transfer from the higher to the lower harmonics is also evident in the analysis of the data taken of the IGV wakes.

Figure 16 shows the first three harmonics of the potential gust upstream of the rotor in the IGV freestream region. The upstream going potential from the rotor blades is dominated by the first-harmonic component; the second and third harmonics contribute slightly. Potential gust harmonics above the third are essentially zero upstream of the rotor. Inspection of the harmonics of the potential gust downstream of the rotor revealed no trends or useful information.

Summary and Conclusions

An experiment was performed in the Purdue Research Axial Fan Stage directed at the acquisition and analysis of data defining forcing functions generated by a rotor, including interactions with the upstream-generated IGV wakes, for application to turbomachine forced-response design systems. With a rotor-relative Mach number of 0.6, unsteady measurements include the rotor wake pressure and velocity fields. First, the decay characteristics of the rotor blade wakes for two IGV–rotor axial spacing values and for rotor wakes measured in the IGV freestream and wake regions were compared to the empirical correlations. Then, after Fourier decomposition, a vortical–potential gust splitting analysis was implemented to

determine the vortical and potential harmonic wake gust forcing functions, both upstream and downstream of the rotor, and to determine the effects of IGV axial spacing and IGV–rotor interactions.

The unsteady velocity and pressure perturbations are very small far upstream of the rotor and grow exponentially with distance toward the rotor. Downstream of the rotor the flow is dominated by narrow viscous wakes. With regard to the comparison of the rotor wake data with the empirical correlations of Majjigi and Gliebe,[3] noticeable differences exist in the near rotor wake region, and varying degrees of correlation exist in the far field. IGV–rotor axial spacing had no effect on the rotor wake velocity deficit, and the increased axial spacing resulted in a small semiwake width increase. The effects of the upstream IGV wake interactions with the downstream rotor wakes are noticeable in the rotor near-field region, with the measured semiwake width generally larger and the velocity deficit smaller than those predicted by the correlation. Also, in the far field, the IGV–rotor wake interaction caused a reduction in the rotor wake velocity deficit and the semiwake width. The nondimensional wake width appears to increase linearly with distance, and the rate of growth appears to be reduced by the IGV wakes.

Application of the splitting analysis shows that the gust is predominantly vortical downstream of the rotor and the rotor upstream unsteady velocity perturbation predominantly potential. The vortical gust first-harmonic magnitude is generally constant in the rotor far field, as predicted by the theory. However, it is not constant in the region near the rotor. Also, decreasing the IGV–rotor axial spacing results in an increase in the magnitude of the vortical gust constant D_1^*, particularly in the near-wake region. The IGV wakes significantly affect the rotor vortical gust component, with the rotor vortical gust magnitude D_n^* much larger in the IGV freestream than in the IGV wake region for all harmonics. In both the IGV wake and freestream, the vortical gust magnitude of the first two harmonics is relatively constant, as predicted by the theory. The higher harmonics (above the third) decay as a result of viscous diffusion that would not be present were the flow inviscid. A slight increase in the far field of the first two harmonics can be explained as the transferal of energy from the higher harmonics to the lower harmonics as the wakes decay.

The potential effects are quite strong immediately upstream of the rotor and relatively small immediately downstream because the steady differential pressure on an airfoil is greatest near the leading edge and decreases to zero at the trailing edge to satisfy the Kutta condition. The decay of A_1^* upstream of the rotor compares well with the rate expected from theory. The upstream going potential from the rotor blades is dominated by the first-harmonic component; the second and third harmonics add small contributions. Decreasing the IGV–rotor spacing increases the magnitude of the potential gust constant A_1^*, both upstream and downstream of the rotor, but the effect is much larger downstream of the rotor. Also, the IGV wakes have only a small effect on the axial behavior of A_1^*, both upstream and downstream of the rotor.

Acknowledgment

This research was sponsored by the GUIde Consortium on Bladed Disk Forced Response.

References

[1]Mugridge, B. D., and Morfey, C. L., "Sources of Noise in Axial Flow Fans," *Journal of the Acoustical Society of America*, Vol. 51, No. 5, Pt. 1, 1971, pp. 1411–1426.

[2]Lakshminarayana, B., and Davino, R., "Mean Velocity and Decay Characteristics of the Guide Vane and Stator Blade Wake of an Axial Flow Compressor," *Journal of Engineering for Power*, Vol. 102, Jan. 1980, pp. 50–60.

[3]Majjigi, R. K., and Gliebe, P. R., "Development of a Rotor Wake/Vortex Model, Vol. 1—Final Report," NASA CR 174849, 1984.

[4]Chiang, H. D., and Kielb, R. E., "An Analysis System for Blade Forced Response," American Society of Mechanical Engineers, Paper 92-GT-172, June 1992.

[5]Henderson, G. H., and Fleeter, S., "Forcing Function Effects on Unsteady Aerodynamic Gust Response Part 1: Forcing Functions," American Society of Mechanical Engineers, Paper 92-GT-174, June 1992.

[6]Manwaring, S. R., and Wisler, D. C., "Unsteady Aerodynamics and Gust Response in Compressors and Turbines," American Society of Mechanical Engineers, Paper 92-GT-422, June 1992.

[7]Feiereisen, J. M., Montgomery, M. D., and Fleeter, S., "Unsteady Aerodynamic Forcing Functions: A Comparison Between Linear Theory and Experiment," American Society of Mechanical Engineers, Paper 93-GT-141, June 1993.

[8]Goldstein, M. E., "Unsteady Vortical and Entropic Distortions of Potential Flows Around Arbitrary Obstacles," *Journal of Fluid Mechanics*, Vol. 89, Pt. 3, 1978, pp. 433–468.

[9]Walker, G. J., and Oliver, A. V. R., "The Effect of Interaction Between Wakes from Blade Rows in an Axial Flow Compressor on the Noise Generated by Blade Interaction," *Journal of Engineering for Power*, Vol. 94, Oct. 1972, pp. 241–248.